Stem Cell Reports
Article

ISSCR

OPEN ACCESS

# Retinoic acid signaling guides the efficiency of inner ear organoid-genesis and governs sensory-nonsensory fate specification

R. Keith Duncan,[1,2,4,5,*] Liqian Liu,[1] Mo Moyer,[1] Andrew Wylie,[1,3] Ranya Dano,[1] and Luis Cassinotti[1]
[1]Department of Otolaryngology – Head and Neck Surgery, Kresge Hearing Research Institute, University of Michigan, Ann Arbor, MI, USA
[2]Veterans Affairs Ann Arbor Health System, Ann Arbor, MI, USA
[3]Present address: Case Western Reserve School of Medicine, Cleveland, OH, USA
[4]Senior author
[5]Lead contact
*Correspondence: rkduncan@umich.edu
https://doi.org/10.1016/j.stemcr.2025.102671

## SUMMARY

Inner ear organoid development—from germ layer to otic vesicle (OV) formation—relies on timed chemical cues to recapitulate major signals *in vivo*. In contrast, later stages of differentiation—from OV to organoid formation—are self-guided, even though these stages are modulated by several key morphogens *in vivo*. We sought to elucidate additional morphogens that might improve culture efficiency and influence cell fate decisions. Using a whole-transcriptomic approach, we identified major differences in native and stem-cell-derived OVs related to anterior-posterior patterning and retinoic acid (RA) signaling. Increasing the level of RA during OV formation in these cultures modulated organoid efficiency, increased nonsensory markers, decreased sensory markers, and decreased hair cell production. The organoid culture platform mimics the exquisite RA sensitivity found in normal inner ear development and provides a tunable system for generating sensory and nonsensory cell types in inner ear organoids.

## INTRODUCTION

Three-dimensional organoid culture systems provide a unique parallel approach to *in vivo* inner ear research. These culture systems are accessible throughout the differentiation process, scalable to high-throughput technologies, and easy to manipulate, opening new paths to study development, disease, therapeutics, and regeneration. To reach their full potential, inner ear organoids (IEOs) must mimic the complexity of inner ear organs and become malleable enough to control cell fate decisions. Recent advances have underscored the capabilities of IEOs to mimic many aspects of native developmental trajectories (Matern and Heller, 2025; van der Valk et al., 2023; Waldhaus et al., 2024). Exogenous chemicals are applied to sequentially guide a three-dimensional spheroid of pluripotent stem cells toward the formation of ectodermal otic intermediates: non-neural ectoderm, preplacodal domains, otic placode, and ultimately formation of otic vesicles (OVs) (Koehler et al., 2013). Almost all sensory and nonsensory cells within the six distinct inner ear organs are derived from the multipotent epithelial progenitor cells of the OV (Groves and Fekete, 2012). In IEO culture paradigms, the formation of OVs within the spheroid marks the transition to a self-assembly phase without the addition of exogenous morphogens to further guide development.

*In vivo*, the spatial organization of inner ear organs is largely defined during morphogenesis of the OV. Diffusible signals from neighboring tissues sequentially pattern the inner ear along major body axes (Groves and Fekete, 2012; Wu and Kelley, 2012). Axial specification is progressive, beginning with an anterior-posterior asymmetry that establishes the neural-sensory domain in the anterior region and nonsensory tissues in the posterior region, save for the posterior crista (Wu and Kelley, 2012). Anterior-posterior patterning is followed by dorsal-ventral segmentation, specifying vestibular-auditory organs, respectively. While recent reports have explored cochlear-vestibular patterning in IEOs by manipulating dorsal-ventral specification (Moore et al., 2023), there has been no attempt to systematically examine the early stage of anterior-posterior patterning, which primarily occurs through the actions of retinoic acid (RA).

RA signaling is indispensable in inner ear development. During a narrow critical window of OV development, low RA exposure in anterior domains guides a prosensory fate, and higher exposure in posterior domains induces nonsensory fates. RA effects are pleiotropic and involve a large number of RA-responsive genes, but only a few definitive RA-target genes have been identified in ear development (Bok et al., 2011; Frenz et al., 2010). Notably, RA dysregulation *in vivo*, whether from genetics or environmental factors, is teratogenic; both excess and deficiency cause ear abnormalities and even complete arrest of inner ear development (Frenz et al., 2010). We hypothesize that RA plays equally important roles in organoid-genesis and in controlling sensory (anterior) versus nonsensory (posterior) fates *in vitro*.

In this study, we fine-tune the IEO protocol with RA to systematically modulate organoid production and develop RA supplementation as a tool for shifting between sensory to nonsensory cell fates. An examination of the transcriptome of isolated OVs from embryonic mouse compared

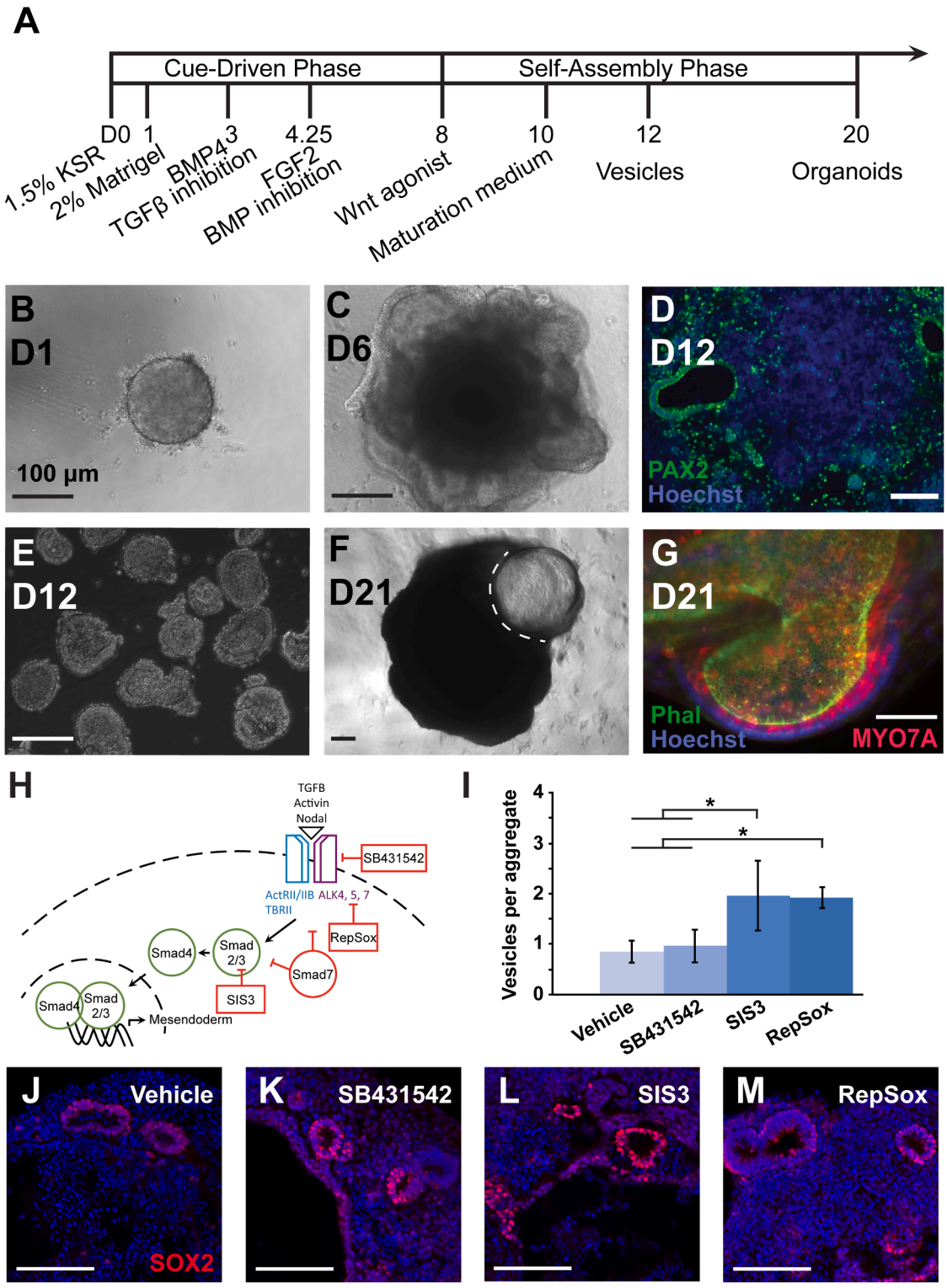


**Figure 1. Generation of inner ear organoids**

(A) The timeline of IEO formation includes a cue-driven phase that generates definitive ectoderm with the addition of Matrigel, non-neural ectoderm with BMP4 and TGF-β inhibition, otic placode with FGF2 and BMP inhibition, and OV formation by WNT activation. A subsequent self-assembly phase ultimately generates IEOs.

*(legend continued on next page)*

to that of age-matched IEO cultures confirmed dysregulation of anterior-posterior pattern specification in the cultures and pointed to the involvement of RA in contributing to organoid heterogeneity and dysmorphogenesis, where some OVs fail to mature into large cystic organoids. Our data replicate the exquisite sensitivity of early stages of inner ear development to spatiotemporal perturbations in RA level and definitively show that systematic variations in RA level tip the balance from sensory to nonsensory domain formation. Consequently, gaining control over RA signaling may lead to rationale approaches for enhancing hair cell production or producing specific populations of nonsensory cell types.

## RESULTS

### R1/E mouse ESCs produce otic-vesicle-like and organoid structures

To produce IEOs, we modified a protocol optimized for R1/E mouse embryonic stem cells (ESCs) (DeJonge et al., 2016) (Figure 1A), referring to this culture paradigm as BSFL for the compounds added in the cue-driven phase (i.e., **B**MP4/**S**B431542 treatment at day 3 [D3] and **F**GF2/**L**DN193189 treatment at D4.5). These cultures recapitulated major checkpoints for IEO production, from formation of the initial spheroid on D1 (Figure 1B) to production of a ruffling non-neural ectodermal layer on D6 (Figure 1C) and generation of PAX2-positive OV-like structures by D12 (Figure 1D). These OVs could be released from the surrounding aggregate (Figure 1E), facilitating downstream analysis of their transcriptomic profiles. Within intact aggregates, the vesicles themselves expanded in size by D20, often becoming large, protruding fluid-filled cysts (Figure 1F) with MYO7A-positive hair-cell-like cells (Figure 1G).

### TGF-β inhibition is dispensable for OV production but indispensable for generating IEOs

To examine the efficiency of IEO production, we focused attention on transforming growth factor β (TGF-β) inhibition and the early stages of germ layer formation. OVs were collected from cultures treated on D3 with vehicle control media and one of several TGF-β inhibitors (i.e., SB431542, SIS3, and RepSox) acting at different points in the TGF-β pathway (Figure 1H). SB431542-treated and untreated aggregates produced vesicles on D12 at comparable efficiency; however, RepSox and SIS3 resulted in significantly more vesicles per aggregate ($p < 0.05$) (Figure 1I). Despite differences in efficiency, vesicles from all conditions were similar in size and each expressed the OV marker SOX2 (Figures 1J–1M), as well as otic markers SIX1, ECAD, and PAX2 (not shown). By D20, large, fluid-filled IEO cysts were observed in the SB431542 (11/12 trials), RepSox (7/7 trials), and SIS3 treatment groups (6/7 trials), with no reliable differences in efficiency of IEO production per experiment (Figure S1A). However, RepSox appeared to produce more organoids per aggregate than SB431542 though this was not quantified. Notably, the vehicle control group never produced internal or protruding cysts (0/8 trials). Sensory hair cells were produced in all inhibitor conditions (Figures S1B–S1D), but hair cells were never observed in cultures without TGF-β inhibition.

### Differences in the transcriptomes of derived compared to native OVs involve anterior-posterior fate specification

Based on these observations, we chose to compare the transcriptomes of derived OVs at D12 cultured in BSFL and BFL conditions (without the TGF-β inhibitor SB431542) and benchmark these against a comparable time point in mouse inner ear development, E10.5 OVs (Schaefer et al., 2018). High-quality cDNA libraries (Tables S1 and S2) were processed through our bulk RNA sequencing (RNA-seq) pipeline. In total, over 22,000 genes had measurable expression levels in these samples, and over 10,000 differentially expressed genes (DEGs) were identified in pairwise comparisons (Table S3). The experimental groups organized into distinct clusters with 89% of the variance captured by the first two principal components

(B) Spheroids form by D1.
(C) A ruffled outer epithelial layer of non-neuroectoderm forms by D6.
(D) A cryosectioned D12 aggregate shows PAX2 OVs (green) and Hoechst nuclei (blue).
(E) Examples of isolated OVs.
(F) Protruding (dotted outline) IEO cysts form by D20.
(G) Microdissected IEOs contain patches of sensory epithelia, where phalloidin-labeled hair bundles (green) extend into the lumen from MYO7A-positive hair cells (red; Hoechst nuclei, blue).
(H) A schematic shows mechanisms of TGF-β pathway inhibition.
(I) The efficiency of OV production on D12 is shown for aggregates treated with different TGF-β inhibitors on D3. *$p < 0.05$; mean ± one standard deviation (SD). In each independent experiment ($n$), OV counts were made from 32 aggregates. $n = 8$ vehicle, 8 SB431542, 5 SIS3, and 5 RepSox.
(J–M) Cryosections from D12 aggregates in each treatment condition show SOX2 OVs (red) and Hoechst nuclei (blue). Scale bars, 100 μm.
See also Figure S1.

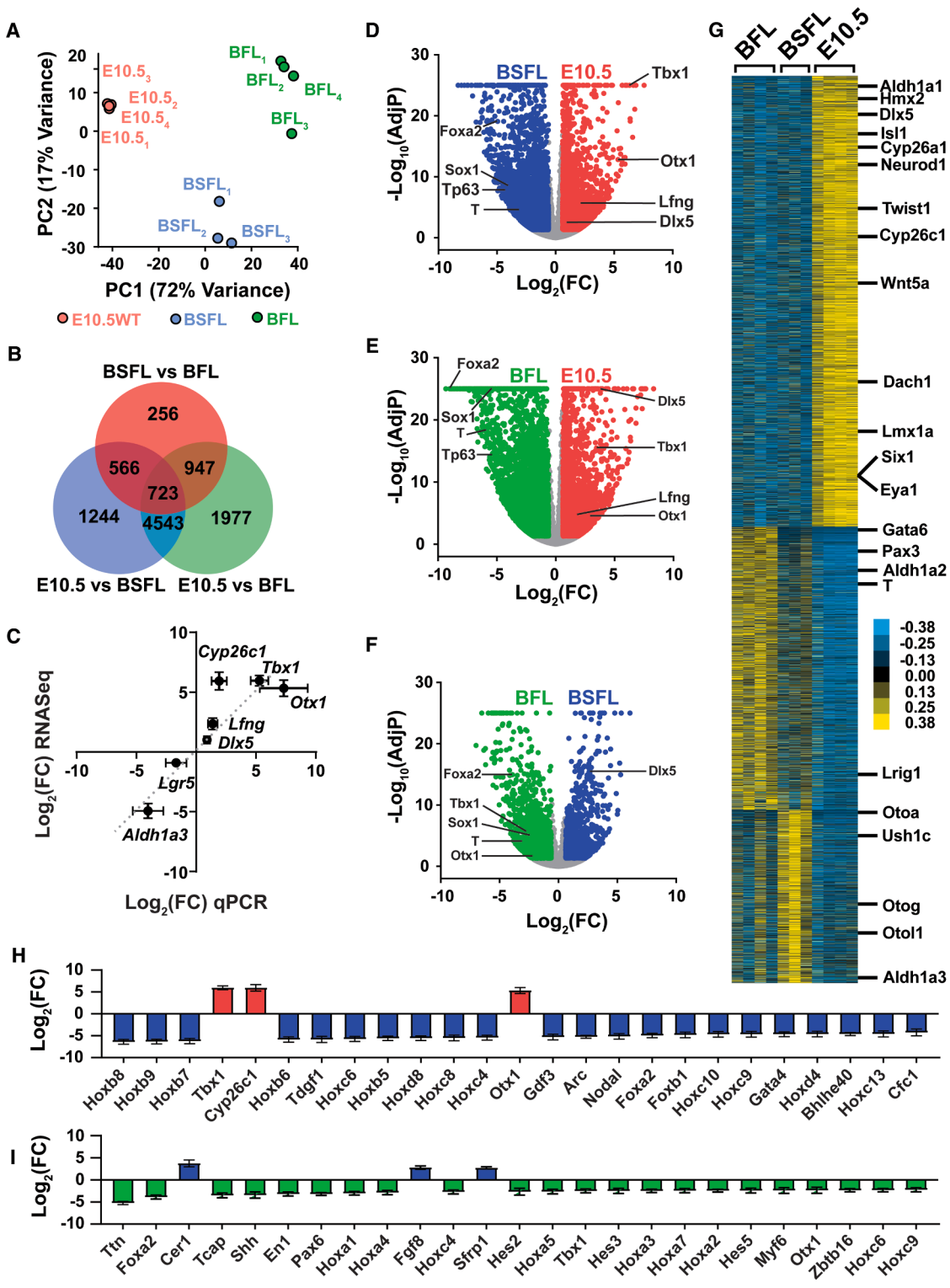


**Figure 2. Bulk RNA-seq analysis of native E10.5 OVs compared with stem-cell-derived OVs at D12 in BSFL and BFL cultures**

(A) Principal-component analysis illustrates clustering of samples by condition, with some greater separation within culture conditions.

(B) Venn diagram shows the DEGs identified in pairwise comparisons of all conditions.

*(legend continued on next page)*

(Figure 2A). Clusters formed by BFL and BSFL OVs—pooled from individual cultures—showed a greater spread compared to E10.5 OVs, indicating considerable between-culture variability. A heatmap from hierarchical clustering illustrated the close relationship between BSFL and BFL samples compared to E10.5 (Figure S2A). These relationships were corroborated by a Venn diagram of DEGs from pairwise comparisons (Figure 2B), where differences were greatest in the native-cultured comparisons and smallest between BSFL and BFL. A large number of DEGs (over 5,000) were common to the E10.5-BFL and E10.5-BSFL comparisons, reflecting a fundamental difference between *in vivo* and *in vitro* samples. Differences in gene expression were validated by quantitative polymerase chain reaction (qPCR) using several key markers (Figure 2C) (linear regression slope 0.94, correlation coefficient 0.79, Pearson's test $p < 0.01$).

To categorize the DEGs further, we generated volcano plots of up- and downregulated genes (Figures 2D–2F, S2B, and S2C). A selection of genes are annotated on the volcano plots representing markers for otic placode (*Lfng*, *Dlx5*, *Otx1*, and *Tbx1*), mesendodermal fate (*T* and *Foxa2*), neuroectoderm (*Sox1*), and non-neural ectoderm/epidermis (*Trp63*) (Burton et al., 2004; Kwon et al., 2010; Laurikkala et al., 2006; Morsli et al., 1999; Ohta et al., 2016; Vitelli et al., 2003; Vyas et al., 2020). The otic markers are enriched in the native OVs, whereas the mesendodermal markers and other ectodermal markers are enriched in the derived OVs (Figures 2D and 2E), suggesting incomplete conversion to an otic fate in these cultures. Consistent with the lack of TGF-β inhibition in BFL samples, mesendodermal markers were higher in BFL than BSFL (Figure 2F).

Hierarchical clustering of the DEGs revealed three distinct clusters (Figure 2G). The first (top) cluster had the largest number of DEGs enriched in E10.5 OVs and included biomarkers of the dorsal (e.g., *Dlx5*, *Hmx2*, and *Aldh1a1*) (Durruthy-Durruthy et al., 2014; Romand et al., 2006; Wang et al., 2004), medial (e.g., *Dach1* and *Eya1*) (Heanue et al., 2002), and ventromedial (e.g., *Six1*) (Zheng et al., 2003) OV as well as delaminating neuroblasts (e.g., *Isl1* and *Neurod1*) (Radde-Gallwitz et al., 2004) and periotic mesenchyme (e.g., *Wnt5a*, *Twist1*, and *Cyp26c1*) (Noda et al., 2012; Romand et al., 2006). The second largest cluster represented BFL cultures enriched with mesodermal-endodermal markers (e.g., *Gata6*, *Pax3*, and *T/Brachyury*) (Vyas et al., 2020). Finally, the third cluster represented BSFL cultures enriched with several genes associated with nonsensory portions of the inner ear (e.g., *Otoa*, *Otog*, and *Otol1*) (Xu et al., 2016).

Gene ontology (GO) analysis associated with DEGs were filtered using "Elim pruning," and the top 10 terms are listed for each pairwise comparison (Table 1). Several GO terms in the native-culture comparisons are related to high levels of transcriptional activity, cell proliferation, and specification of non-otic tissues, suggesting incomplete programming of otic fates in the cultures. The top GO term in each comparison with E10.5 was "anterior/posterior pattern specification," and many of the top DEGs in this GO term were associated with posterior hindbrain segments (i.e., higher numbered *Hox* genes) (Figure 2H). All *Hox* DEGs except for the anteriorly positioned *Hoxa2* were more highly expressed in BSFL-derived OVs than native tissue (Figure S2B), suggesting posteriorizing factors in the cultures. Notably, "anterior/posterior pattern specification" also appeared as a top GO term in the BSFL-BFL comparison, driven by enrichment of more posterior *Hox* genes in BFL (Figure 2I).

Anterior-posterior patterning involves gradients of RA for segmentation along the body (Niederreither and Dolle, 2008) and in the developing OV (Bok et al., 2011). GO terms related to RA appeared in all group comparisons (marked with * in Table 1). Shifting boundaries of RA synthesis contribute to gradations in *Hox* gene expression, and *Hox* genes with known RA sensitivity were among the top DEGs in BSFL OVs (e.g., *Hoxb5-9*) (Figure 2H) (Flagiello et al., 1997). Additionally, we found the RA metabolizing enzyme *Cyp26c1* to be highest in E10.5 and the synthesizing enzyme *Aldh1a3* highest in BSFL (Figure S2C). These results suggest higher levels of RA signaling *in vitro* compared to *in vivo*. Hence, fine-tuning RA signaling could improve IEO efficiency and tip the balance between anterior-posterior patterns.

(C) The fold-change ($Log_2$(FC)) for select genes is compared between RNA-seq data and qPCR for E10.5 OVs relative to BSFL cultures (mean ± one SD). Dotted line indicates the line of unity.
(D–F) Volcano plots of DEGs for pairwise comparisons show the distribution of up- and downregulated genes. A selection of otic placodal (*Lfng*, *Dlx5*, *Otx1*, and *Tbx1*), mesendodermal (*T* and *Foxa2*), neuroectodermal (*Sox1*), and non-neural ectodermal (*Trp63*) genes are indicated in each panel.
(G) A heatmap from hierarchical clustering is shown with the position of select otic and mesendodermal DEGs. The top 25 DEGs in the "anterior/posterior pattern specification" GO term for biological processes are illustrated by log fold-change for (H) E10.5 compared to BSFL cultures and (I) BSFL compared to BFL cultures (mean ± one SD). In each independent experiment (N), 2 to 6 OVs were pooled from 1 to 3 embryos or 30 to 50 OVs were pooled from 32 to 48 aggregates. $n = 6$ BSFL qPCR, 3 BSFL RNA-seq, 3 E10.5 qPCR, 3 E10.5 RNA-seq. See also Figure S2, Table S3.

**Table 1. Biological processes GO terms**

| Comparison | GO term | Genes (DEG/ALL) | Adjusted *p* value |
|---|---|---|---|
| E10.5 vs BSFL | cell proliferation | 731/1,832 | 1.4E−8 |
| | anterior/posterior pattern specification | 116/225 | 1.7E−7 |
| | positive regulation of myeloid cell differentiation | 51/88 | 7.2E−7 |
| | positive regulation of transcription by RNA polymerase II | 453/1,162 | 1.6E−6 |
| | embryonic organ morphogenesis | 146/311 | 1.9E−6 |
| | cardia muscle concentration | 63/120 | 7.9E−6 |
| | male meiotic nuclear division | 31/49 | 9.3E−6 |
| | synapsis | 29/48 | 1.1E−5 |
| | keratinocyte differentiation | 52/97 | 1.3E−5 |
| | EKR1 and EKR2 cascade | 131/296 | 1.3E−5 |
| E10.5 vs BFL | embryonic organ morphogenesis | 179/311 | 6.7E−14 |
| | anterior/posterior pattern specification | 169/225 | 5.6E−13 |
| | morphogenesis of a branching structure | 140/235 | 7.1E−11 |
| | positive regulation of cell proliferation | 426/885 | 1.9E−10 |
| | ear development | 132/231 | 3.9E−10 |
| | embryonic skeletal system development | 83/134 | 2.3E−9 |
| | muscle organ development | 208/405 | 9.3E−9 |
| | positive regulation of cell differentiation | 484/1,044 | 2.1E−8 |
| | positive regulation of transcription by RNA polymerase II | 520/1,162 | 3.1E−8 |
| | inflammatory response | 294/580 | 3.5E−7 |
| BSFL vs BFL | embryonic organ morphogenesis | 109/307 | 5.0E−23 |
| | embryonic skeletal system development | 58/134 | 5.0E−18 |
| | anterior/posterior pattern specification | 78/223 | 3.7E−17 |
| | cell morphogenesis involved in differentiation | 187/768 | 1.3E−16 |
| | sarcomere organization | 30/51 | 1.8E−14 |
| | muscle organ development | 121/401 | 1.1E−13 |
| | skeletal system morphogenesis | 79/248 | 1.4E−13 |
| | neuron projection guidance | 75/235 | 6.4E−13 |
| | adult behavior | 57/172 | 8.3E−12 |
| | extracellular matrix organization | 76/249 | 1.5E−11 |

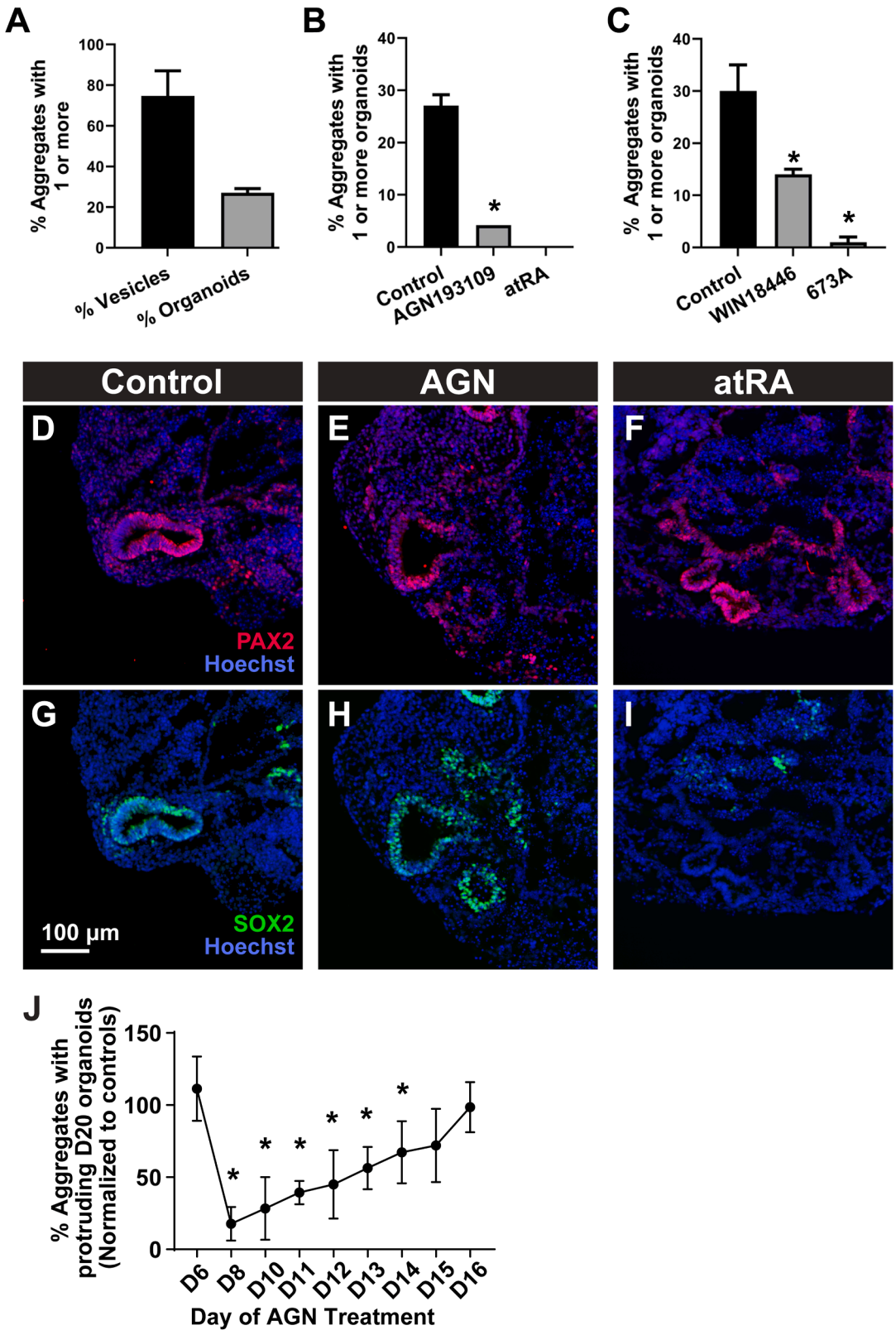


*(legend on next page)*

## Excessive and deficient RA signaling reduces the efficiency of organoid-genesis during a critical time window

*In vivo*, exposure to excessive and deficient RA signaling results in OV dysmorphogenesis and often arrest of inner ear development (Frenz et al., 2010). To test these effects in IEO cultures, we manipulated RA signaling between D8 and D12, in cultures using RepSox as the TGF-β inhibitor since this compound improved culture reliability and efficiency. In control conditions, the efficiency of producing OVs and protruding IEOs was about 75% and 30%, respectively (Figure 3A). Both inhibition of RA receptors (RARs) with the pan-RAR antagonist AGN193109 and the addition of all-*trans* RA (atRA) significantly inhibited organoid production (Figure 3B). Similarly, inhibition of endogenous RA biosynthesis with the Aldh1a2 blocker WIN18446 reduced organoid formation, and widespread inhibition of the Aldh1a family with 673A nearly eliminated organoid production (Figure 3C). Similar to control samples, D12 aggregates treated with AGN193109 produced OVs positive for the otic markers PAX2 and SOX2 (Figures 3D, 3E, 3G, and 3H). However, the addition of atRA eliminated SOX2 expression in the vesicles (Figures 3F and 3I), suggesting one possible mechanism for failed morphogenesis in this condition (Kiernan et al., 2005). Additionally, RA influence occurred in a critical time window like *in vivo* OV development (Bok et al., 2011) (Figure 3J).

## RA responsiveness in derived OVs is variable and asymmetric

Given the sensitivity of native and derived OVs to RA manipulation, we hypothesized that variable endogenous RA activity may limit IEO efficiency in control cultures. Mice with a transgene reporter composed of RA response elements (RAREs) upstream of *lacZ* have been used to monitor RA activity in mouse otic development (Bok et al., 2011). Therefore, we developed a RARE-lacZ ESC line from the progeny of RARE$^{lacZ/lacZ}$ mice [Tg(RARE-Hspa1b/lacZ)12JRT] crossed with wild-type C57BL/6J mice. To validate this model, we verified that adult RARE$^{lacZ/+}$ progeny responded well to acoustic stimuli (Figure 4A), showed normal cochlear morphology (Figure 4B$_1$), and maintained RA reporter activity (Figure 4B$_2$). Over 20 E3.5 blastocysts from the F1 cross were examined for the *lacZ* transgene, and line A6 was selected for analysis (Figure 4C). The RARE-lacZ ESCs showed a log-linear relationship between X-gal intensity and atRA dose, confirming their ability to sensitively report RA activity (Figures 4D and 4E). The RARE-lacZ ESCs were optimized for the IEO protocol, producing OVs, organoid cysts, and sensory hair cells (Figures 4F–4H).

Cultures of RARE-lacZ ESCs in the IEO protocol showed positive X-gal staining as early as culture D9, which became faint and more restricted to OVs at later time points (Figures S3A–S3C). At D8 and D10, RA activity was associated with the aggregate core, distinct from the surrounding placodal epithelium (Figures 4I and 4J). On D12 through D20, RA activity could be found within the OVs and IEOs, but the labeling was highly variable between otic tissues within the same aggregate and was non-uniform around their perimeters (Figures 4K–4N). The addition of 500 nM atRA on D8 increased lacZ expression intensely in whole aggregates at D9 (Figures S3A–S3C), and this was largely due to intense staining of the otic-epibranchial placodal domain (Figures 5A and 5B). The impact of excess atRA was reduced when applied at later time points, consistent with a critical window of RA sensitivity (Figures S3B and S3C).

In sections from D13 to D14 cultures, more intense X-gal labeling was often found in the aspects of the OV facing the outer edge of the aggregate (Figures 5C and 5C′). After treating with 500 nM atRA from D8-D12, the stain was more intense and uniform around the OV (Figures 5D and 5D′). The perimeter of the OVs was also smaller in atRA-treated cultures than controls—164.7 ± 13.6 μm and 284.9 ± 16.5 μm, respectively (mean ± one standard error; $p < 0.0001$). We measured the X-gal intensity around the perimeter of the vesicles and transformed the data to polar coordinates (Figures S4A and S4B). The

**Figure 3. RA modulation of organoid efficiency**

(A) The percentage of aggregates with one or more visible OVs (% Vesicles) at D12 or protruding organoids at D20 (% Organoids) is shown for control cultures. The efficiency of producing protruding organoids by D20 is shown for vehicle controls and (B) samples treated with the pan-RAR antagonist AGN193109 or 500 nM atRA and (C) those treated with Aldh1a inhibitors WIN18446 or 673A; all treatments applied on D8 through D12. *$p < 0.05$ in unpaired t tests compared to controls.

(D–I) Expression of OV markers PAX2 (red) and SOX2 (green) with Hoechst (blue) in cryosections from D12 aggregates, representative of over 20 aggregates per condition in three independent preparations.

(J) A critical window of RA sensitivity extends from D8 to D14, a time when otic placode and vesicle intermediates are being produced. The efficiency of producing protruding organoids by D20 is shown for cultures treated with AGN193109 for 24 h on the day indicated. Data were normalized to average control values. One-way ANOVA revealed a significant effect over time ($p < 0.0001$) with *$p < 0.05$ in post-hoc pairwise comparisons to controls. (A–C, J) Mean ± one SD with $n = 3–5$ independent samples per condition and 40–50 aggregates per sample. Scale bars, (D–I) 100 μm.

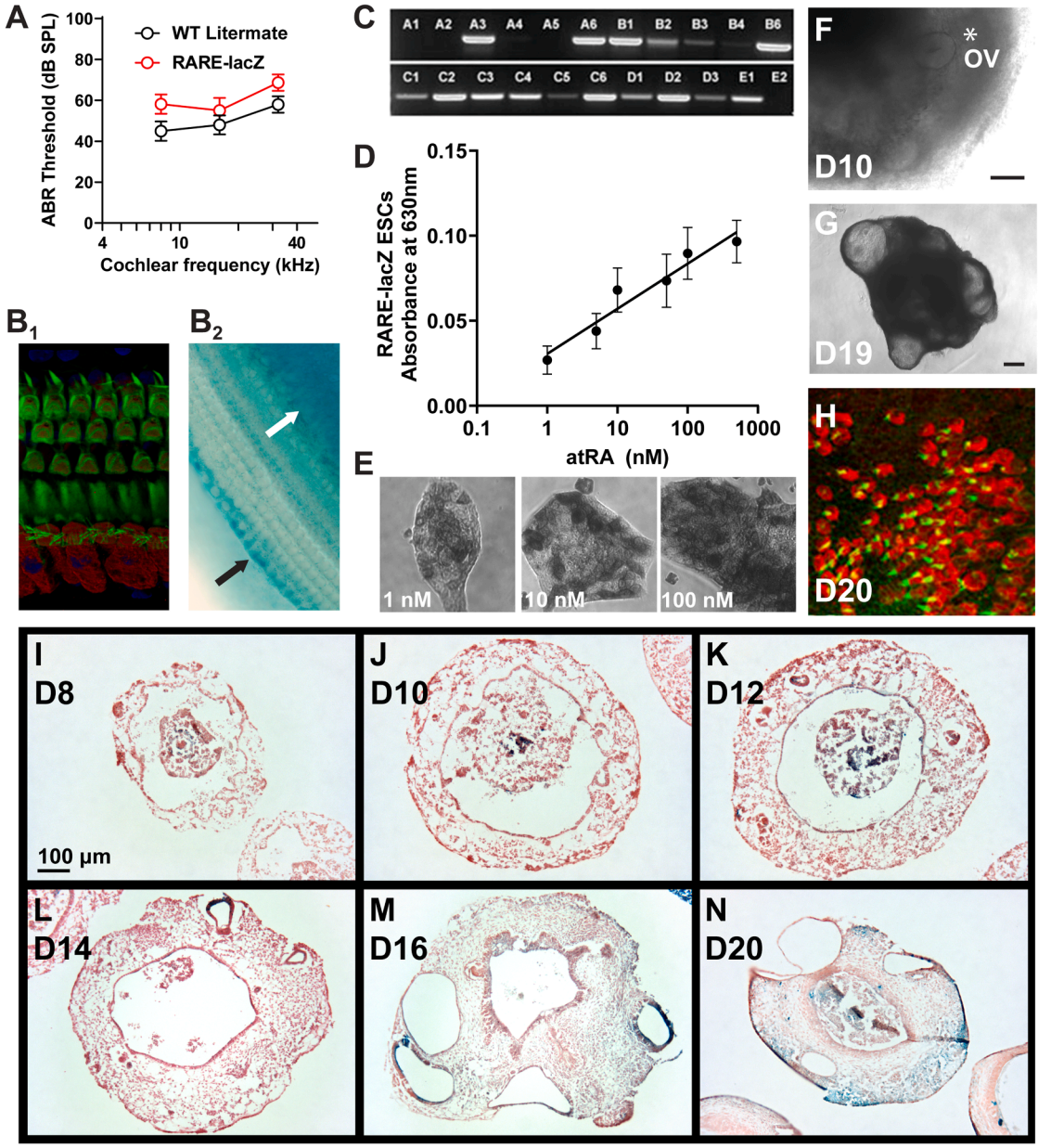


**Figure 4. Development of RARE-lacZ reporter ESCs and IEOs**

(A) Auditory brainstem response thresholds for 4-week-old RARE$^{lacZ/+}$ mice ($n = 11$) and wild-type (WT, $n = 5$) littermate controls ($p < 0.05$, one-way ANOVA across genotype). Mean ± one SD.

Whole mounts of middle cochlear turns from RARE$^{lacZ/+}$ mice were stained by ($B_1$) immunofluorescence with MYO7A (red) and phalloidin (green) or ($B_2$) X-gal; arrows indicate positive Xgal stain in supporting cells bordering the outer hair cells (black arrow) and in the spiral limbus (white arrow).

(C) Genotyping PCR for lacZ is shown for 22 mouse ESC lines from RARE$^{lacZ/+}$ blastocysts. Clone A6 was chosen for follow-up experiments.

(D) Absorbance from X-gal staining of line A6 exposed to a 24-h atRA dose at various concentrations. Log-linear regression correlation coefficient ($R^2$) was 0.94. Mean ± one SD.

(E) X-gal signal increased with RA dose. The RARE-lacZ ESCs were able to generate (F) OVs (marked with asterisk) and (G) IEOs with (H) MYO7A (red) and phalloidin (green) labeled hair cells.

(I–N) X-gal stain (blue) along with Fast Red counterstain in representative thin sections are shown at indicated culture time points. Images are representative of two independent cultures and more than 10 independent aggregates per time point. Scale bars, (F–G, I–N) 100 µm.

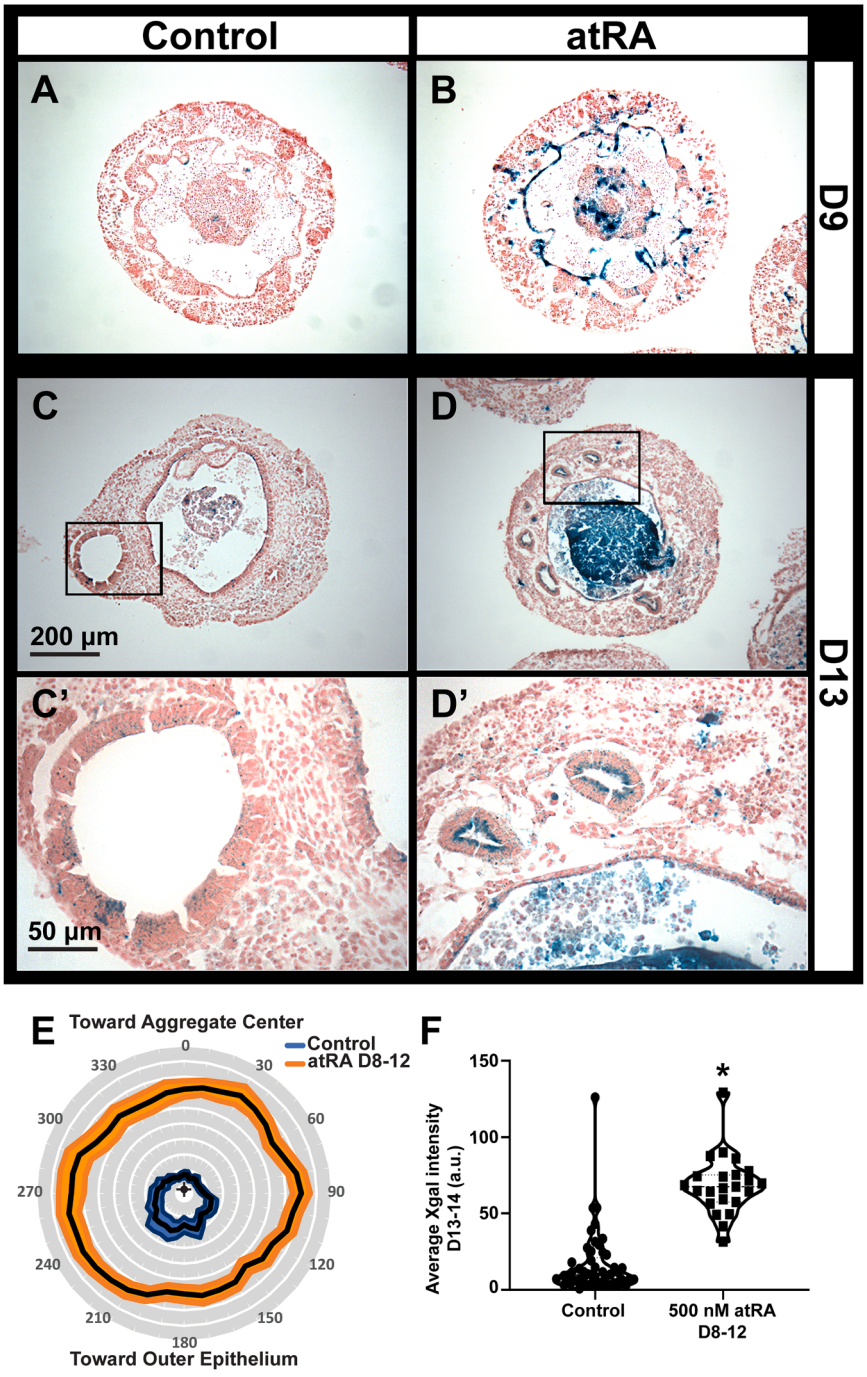


**Figure 5. Asymmetry in RA responsiveness and impact of exogenous RA on RARE-lacZ reporter expression**

Representative images from (A and B) D9 and (C and D) D13 preparations are shown for X-gal (blue) and Fast-Red-stained sections from (A and C) control preparations and (B and D) those treated with 500 nM atRA from D8 to D12. (C′, D′) Boxed insets from (C and D) at higher magnification.

(E) Mean X-gal intensity for control ($n = 49$ from three independent experiments) and atRA-treated vesicles ($n = 23$ from three independent experiments) plotted on polar coordinates relative to the aggregate center. Mean indicated by the center solid black line with one standard error shown in filled areas around the mean. One-way ANOVAs for each condition revealed a significant difference in intensity with respect to polar orientation for controls ($p < 0.01$) but not for those treated with atRA ($p > 0.05$).

(F) The average X-gal intensity throughout each OV is shown by dot plot with significance tested by unpaired t test; $^*p < 0.0001$. Scale bars,: (A–D) 200 µm and (C′, D′) 50 µm. See also Figures S3 and S4.

average intensity for control vesicles was asymmetric and greatest toward the outer aggregate epithelium, whereas atRA treatment caused more intense and uniform staining (Figure 5E). The overall intensity of X-gal in control vesicles was highly variable, with average intensity in some samples matching that of atRA-treated vesicles (Figure 5F)—conditions that would arrest organoid-genesis (see Figure 3B).

## Systematic variations in RA level regulate organoid efficiency and sensory-nonsensory fate

To gain control over RA activity, we sought to suppress endogenous RA synthesis and add atRA at various doses. Due to some toxicity caused by the commercial 673A pan-Aldh1a family inhibitor, we used a custom inhibitor specific to Aldh1a1-3 (compound 69 in Huddle et al., 2018 synthesized by the UM Vahlteich Medicinal

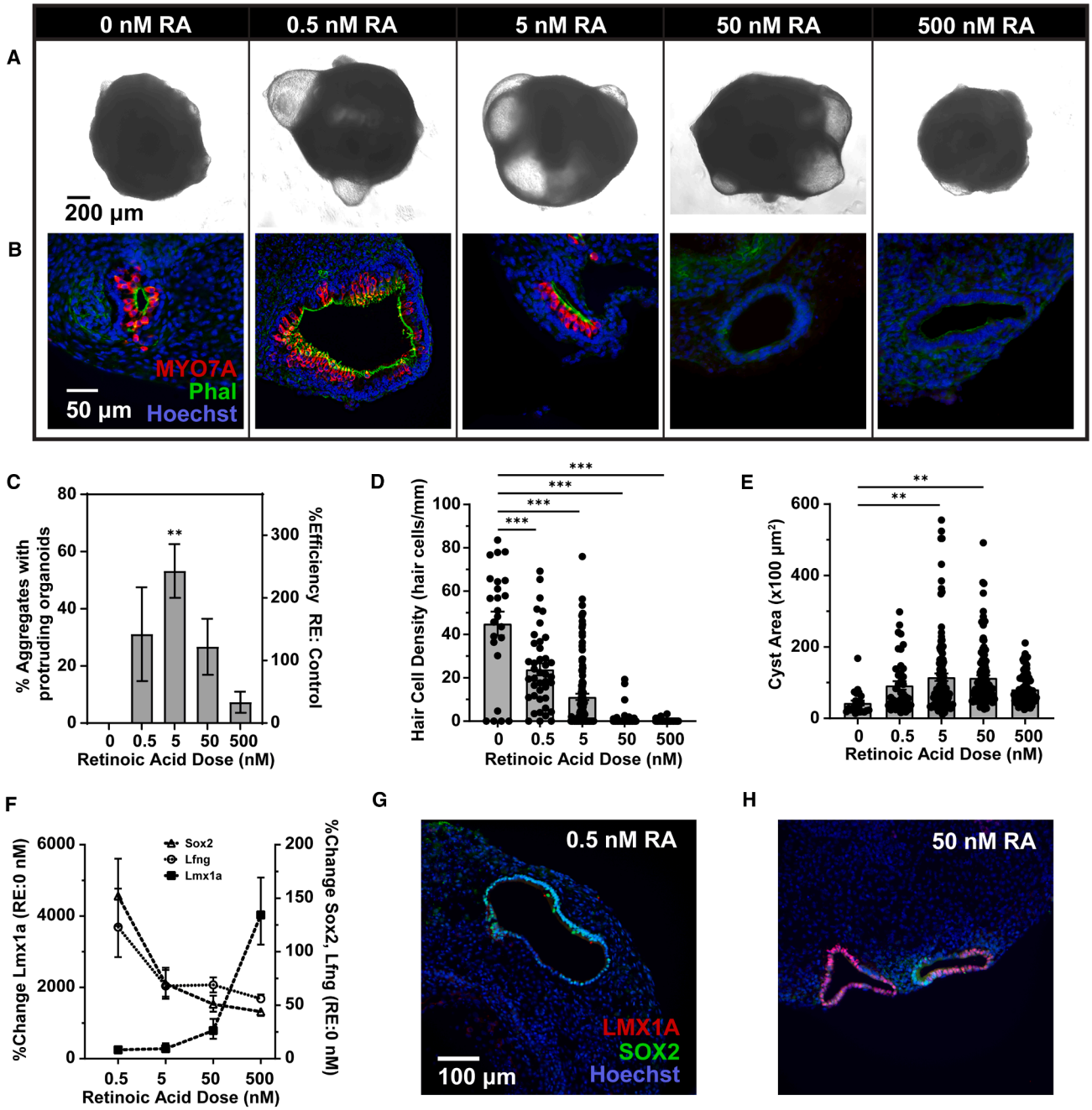


**Figure 6. Effects of controlled exposure to exogenous atRA on sensory-nonsensory cell fate in IEOs**

(A) Example images from aggregates treated with the Aldh1a1-3 inhibitor 646 from D7–D12 while adding various concentrations of exogenous atRA on D8–D12.

(B) Representative immunofluorescence images are shown for cryosections stained for MYO7A (red), phalloidin (green), and Hoechst (blue).

(C) Efficiency of the production of protruding cyst-like organoids, shown as both the % aggregates containing one or more organoids and the percentage relative to control cultures. Mean ± SD. *n* = 3 independent samples per condition and 80–94 aggregates per sample.

(D) Hair cell density and (E) IEO cyst area are shown for thin sections from D20 aggregates under the various RA conditions. Hair cell number was quantified as density, normalized by the perimeter of the cyst within the section. Dots indicate individual data points on top of bar graphs of mean ± one standard error. *n* = 24 to 125 organoids from 13 to 32 aggregates per condition.

*(legend continued on next page)*

Chemistry Core as compound CCG-263646 or 646 for short). Inhibitor 646 was applied during placode and OV formation from D7 to D12 while atRA was added from D8 to D12 at doses from 0 to 500 nM. Exemplary images of D20 aggregates show a non-monotonic dose dependency on production of protruding cystic IEOs (Figure 6A) with decreasing production of MYO7A-positive hair cells as RA levels increased (Figure 6B). Intermediate levels of atRA increased the efficiency of generating large protruding organoids by about 2.5-fold compared to controls (Figure 6C). Hair cell density steadily decreased with atRA level, but cyst size peaked at moderate atRA levels (Figures 6D and 6E). Increasing atRA dose resulted in decreasing sensory (i.e., *Sox2* and *Lfng*) and increasing nonsensory (i.e., *Lmx1a*) gene expression in whole aggregates from D12 cultures (Figure 6F) (one-way ANOVA on ΔCt values, *Sox2* $p < 0.01$, *Lfng* $p < 0.05$, *Lmx1a* $p < 0.0001$). These effects were also observed in D12 cryosections using antibodies to LMX1A and SOX2 (Figures 6G and 6H). At low levels of RA, only SOX2-positive prosensory domains were found in D12 OVs, while at higher doses the OVs showed increasing amounts of LMX1A nonsensory domains. By controlling RA exposure, IEO fate could be systematically shifted from sensory to non-sensory fates, but the size and efficiency in producing large organoid cysts appeared to occur at intermediate RA levels.

## DISCUSSION

In this study, parallels between IEO differentiation and mouse otic development were explored with an eye toward improving culture efficiency and identifying factors to tailor cell type. We first identified TGF-β inhibition as dispensable for OV formation but indispensable in the formation of mature hair-cell-containing organoids. Our data suggest an opportunity to further optimize the IEO protocol with the concentration, duration, and type of TGF-β inhibitor. First, attenuation of TGF-β signaling is necessary for suppression of mesendodermal fate and the formation of anterior ectoderm in mice (Jia and Meng, 2021), but culture-derived OVs showed persistent upregulation of non-ectodermal genes, suggesting incomplete suppression of mesendodermal fates. Furthermore, OV-like structures formed in the absence of TGF-β inhibitors showed even greater expression of mesendodermal and posterior markers. It remains unclear whether these effects were through direct action of TGF-β signaling on OVs or paracrine signaling from mesendodermal tissue. Second, the improved efficiency of vesicle formation with RepSox and SIS3 supports these inhibitors as useful alternatives to SB431542, with RepSox becoming a key part of our IEO protocol in prior reports (Hocevar et al., 2021; Waldhaus et al., 2024). Notably, RepSox shows greater specificity for ALK5 receptor subunits compared to ALK4 and ALK7, and these receptors exhibit differential affinities for TGF-β family ligands. Thus, a deeper dive into the differential role of these receptor pathways may reveal new roles for TGF-β family ligands on OV differentiation and new opportunities to improve the IEO protocol.

Despite the influence of TGF-β on IEO competence, the major differences in native and cultured OV transcriptomes indicated dysregulation of anterior-posterior fate and RA signaling in the cultures. Anterior-posterior domains are established in the mouse otic cup/OV by a spatiotemporal wave of RA during a narrow critical window between E8.75 and E.9.5 (Bok et al., 2011). Lower exposure to RA gives rise to anterior neurosensory domains, while higher exposure generates posterior nonsensory domains. Large perturbations in RA signaling—either extreme excess or deficiency—results in OV dysmorphogenesis (Frenz et al., 2010), suggesting that a delicate balance of RA signaling and mixture of sensory-nonsensory domains is required for normal inner ear organogenesis. Our data replicate the critical window of RA sensitivity at the time of otic placode/OV formation, the systematic shift between sensory and nonsensory domains with RA exposure level, and the teratogenic effects of RA excess and deficiency on organoid-genesis. Evidence of aberrant endogenous RA signaling included (1) reductions in organoid efficiency upon receptor inhibition and blockade of endogenous RA synthesis, (2) a dose-dependent effect on efficiency when blocking select RA synthesis enzymes, and (3) RARE-lacZ responsivity that often matched OVs treated with teratogenic levels of RA. Taken together, we suggest a modification to the IEO protocol, with an RA dose between 0.5 and 5 nM applied between D8 and D12 to maximize organoid production, cyst size, and robust hair cell production. More experiments are required to explore RA sensitivity within this range and to quantify hair cell production

(F) Quantitative PCR data are shown for the % change in prosensory markers *Lfng* and *Sox2* and the nonsensory marker *Lmx1a* relative to the 0 RA condition (646 in the absence of atRA). $n = 3–6$ independent samples per condition and 9–16 aggregates per sample. Mean ± SD. (G and H) Thin sections from D20 IEOs are shown for the sensory domain marker SOX2 (green) and nonsensory marker LMX1A (red), counterstained with Hoechst under low-dose RA (646 + 0.5 nM atRA) and high-dose RA (646 + 50 nM atRA). (C–E) $*p < 0.05$, $**p < 0.01$, and $***p < 0.001$ in post-hoc pairwise comparisons compared to control in (C) and 0 RA condition in (D and E). Scale bars, (A) 200 μm, (B) 50 μm, and (G and H) 100 μm.

with more precise measurements, such as counts from full reconstructions of IEOs or from fluorescence-activated cell sorting using hair cell markers.

In addition to changes in efficiency and cell fate, RA impacted IEO morphology with moderate doses, giving rise to large protruding organoid cysts. We found embedded, internal IEOs at all RA doses, but only moderate levels of RA generated protruding cysts. Nothing is currently known about the composition and homeostasis of the luminal fluid of embedded or protruding organoids. However, it seems inescapable that the composition of ion channels and transporters is unique between these two types of cysts, with our data suggesting that composition is regulated by RA. Changes in ion flux across the epithelia would be accompanied by mechanical effects on the epithelium. The resulting changes in the mechanobiology could then feedback onto cell fate decisions, as appears to be the case in other organoid systems (Nauryzgaliyeva et al., 2023).

Though RA signaling clearly regulates organoid-genesis, the site of RA synthesis and source of endogenous retinoids is unclear. In this study, culture-derived OVs overexpressed the RA synthesis enzyme *Aldh1a3* while downregulating the metabolizing enzyme *Cyp26c1* compared to native OVs. Similarly, a recent single-cell atlas of D11 OVs (Matern and Heller, 2025), probed using the public gEAR database (Orvis et al., 2021), showed high levels of *Aldh1a3* in the cultured OVs, with little RA-related gene expression in non-otic cell types (e.g., neurons, mesenchyme, epidermis, and mesendoderm). Thus, synthesis likely occurs in the OV and leads to autocrine regulation rather than paracrine signaling from peri-otic cell types. The source of retinoid precursors remains unknown, but some components of the culture paradigm are still ill-defined, such as the animal-derived artificial extracellular matrix Matrigel. If Matrigel is the source of retinoids, lot-to-lot variations in gel composition and therefore retinoid level could be a contributing factor to heterogeneity in IEO culture outcomes. Future iterations of the IEO protocol should explore alternative chemically defined hydrogels modified with extracellular matrix peptides.

In summary, we have demonstrated that TGF-β and RA—two morphogens that show considerable crosstalk in development (Xu and Kopp, 2012)—have a profound impact on the production of IEOs. Future investigations should attempt to tease apart the intersections of these pathways in organoid-genesis. Understanding how these, and other, signaling events influence efficiency and cell fate at each stage will be especially beneficial to inner ear research as it may lead to generating large quantities of tailored inner ear cell types for *in vitro* studies and for developing *in vivo* cell replacement therapy. The study also offers Sox2 as another key player in teratogenicity from excess RA. Increasing the dose of atRA decreased SOX2-positive sensory domains while expanding LMX1A-positive nonsensory domains. These manipulations offer a novel platform for interrogating RA target genes and systematically generating a wide range of sensory and nonsensory otic cell types. The ability to expand the nonsensory domains formed in IEOs could be useful for examining the roles of deafness genes specific to inner ear nonsensory cell types (e.g., *Kcnj10* and *Slc26a4*).

## MATERIALS AND METHODS

### Mouse and cell models

The study utilized R1/E mouse ESCs and a RARE-lacZ reporter line. The RARE-lacZ ESC line was established in collaboration with the University of Michigan Transgenic Animal Core, crossing RARE-lacZ [Tg(RARE-Hspa1b/lacZ) 12Jrt] mice with wild-type C57BL/6J mice. All animal procedures were approved by the Institute Animal Care and Use Committee at the University of Michigan (PRO00008446 and PRO00007879). Embryos were harvested from timed pregnant dams with the plug date referencing E0.5. Blastocysts from E3.5 embryos were expanded on feeder layers of mitotically inactivated mouse embryonic fibroblasts before adapting to feeder-free culture conditions.

### Mouse ESC cultures

For stem cell maintenance, colonies were cultured in feeder-free conditions on 0.1% gelatin in 2i culture media (1:1 mixture of Advanced DMEM/F-12 and Neurobasal, 0.5X B-27 without vitamin A, 1X N-2, and 1X GlutaMAX with 1,000 U/mL LIF, 1 μM PD0325901, and 3 μM CHIR99021). Colonies were dissociated to single cells with TrypLE Express for maintenance and producing aggregates.

### Differentiation protocol

As described elsewhere (Hocevar et al., 2021; Schaefer et al., 2018; Waldhaus et al., 2024), IEO cultures were established on D0 by aggregating a suspension of ESCs in round-bottom 96-well microplates seeded at a density of 3,000 cells per well in ectodermal differentiation medium (GMEM, 1.5% KnockOut serum replacement, 15 mM HEPES, 1X non-essential amino acids, 1 mM sodium pyruvate, and 0.1 mM β-mercaptoethanol). On D1, growth-factor-reduced Matrigel (2%) was added. On D3, 10 ng/mL BMP4 was added alone or with TGF-β inhibition using 1 μM SB431542, 3 μM SIS3, or 1 μM RepSox. On D4.5, 1 μM LDN193189 and 100 ng/mL FGF2 were added. Aggregates were transferred into maturation medium on D8 (Advanced DMEM/F-12, 1X N-2 supplement, 15 mM

HEPES, and 1X GlutaMAX) with 1% Matrigel and 3 μM CHIR99021, with daily half-media exchanges from D10 onward.

### Isolation of otic vesicles

Pregnant C57BL/6 dams at E10.5 were euthanized, and uterine horns were removed. A window was cut in the epithelium adjacent to the second branchial arch of each embryo, and vesicles were teased away from periotic mesenchyme and flash-frozen. For organoid cultures, R1/E aggregates at D12 were incubated in 1X collagenase/hyaluronidase at 37°C and triturated gently every 15 min. After 45 min, the mixture was filtered through a 40-μm cell strainer, inverted, washed with DMEM/F-12 to retrieve vesicles, and flash-frozen. To calculate the efficiency of vesicle production, the number of isolated vesicles was normalized by the number of aggregates in the sample.

### RNA analysis

Total RNA was extracted using RNeasy Mini Kits (Qiagen) and transferred to the UM Advanced Genomics Core for library preparation and sequencing. RNA input was assessed for quality and quantity using an Agilent Bioanalyzer 2100 and NanoDrop ND-1000 spectrophotometer. qPCR was achieved using SYBR Green chemistry, Platinum Taq DNA Polymerase, and custom primer sets with amplification efficiencies between 90% and 110%. Fold-change was calculated by $2^{-\Delta\Delta Ct}$.

For bulk RNA-seq, cDNA libraries were prepared from 100 ng total RNA per sample using a TruSeq RNA Sample Prep Kit v2. Library quality was confirmed by Agilent 2200 TapeStation and qPCR before sequencing. The Illumina HiSeq-2500 platform was used to perform V4 single end, 50 bp sequencing of libraries. Samples were sequenced in duplicate, with each sample loaded in two separate lanes.

Data analysis was performed on Fastq output files using Galaxy v18.01 (Afgan et al., 2018). The quality of base calls was assessed using FastQC v0.69 (Andrews, 2010). Reads were trimmed and filtered with Cutadapt v1.14 (Martin, 2011). Low-quality base calls (Phred <20) and short reads (<20 bp) were removed. Reads were aligned to the mm10 genome assembly with HISAT2 v2.0.5.2 (Kim et al., 2015). The resulting BAM files were merged to combine data from duplicate lanes. Data were converted to raw counts with the HTSeq v0.6.1 using Ensembl annotations (Anders et al., 2015), which were then normalized for differential expression analysis using DESeq2 v2.11.39 (Love et al., 2014). Normalized counts from DESeq2 were processed using Cluster 3.0 (de Hoon et al., 2004) for preparation of heatmaps using Java TreeView (Saldanha, 2004). Functional analysis based on GO enrichment was performed on HTSeq counts within iPathwayGuide (Donato et al., 2013; Draghici et al., 2007), setting threshold $p$ values at $< 0.05$ adjusted for false discovery rate and $Log_2FC > 0.6$.

### Auditory brainstem response

Auditory brainstem responses (ABRs) were performed on 1-month-old anesthetized mice (100 mg/kg ketamine and 20 mg/kg xylazine, intraperitoneally [i.p.]), as described elsewhere (Cassinotti et al., 2024). Briefly, acoustic stimuli were delivered through a closed acoustic system with two sound sources and a condenser microphone. Three needle electrodes were placed into the skin along the dorsal midline at the neural crest, behind the left pinna, and at the base of the tail. ABR potentials were evoked with 5-ms tone pips delivered to the eardrum at 8, 16, and 32 kHz. The response to alternating stimulus polarity was amplified (10,000X), filtered (0.3–3 kHz), and averaged (1024 responses). Sound pressure level was raised in 5 dB steps. Thresholds were determined as the lowest level with a reliable first peak of the ABR waveform.

### Whole-mount preparations, cryosections, and immunostaining

Neonatal $RARE^{lacZ/+}$ mice (6 days old) were euthanized under anesthesia, and the bony cochlear duct isolated into fixative (4% paraformaldehyde) for several hours at room temperature. The organ of Corti was microdissected from the cochlear duct and maintained in PBS. Whole aggregates from cultures were fixed similarly, preserved in 30% sucrose, embedded in OCT, and frozen on dry ice. OCT blocks were sectioned using a Leica 3050S cryostat at 10–12 μm thickness. In some cases, IEOs were dissected from fixed aggregates for later staining.

For immunostaining, cochlear whole mounts, dissected IEOs, or cryosections were blocked in 10% normal donkey serum and permeabilized in 0.1% Triton X-100 before incubating overnight with primary antibodies in a 1:1 solution of PBS and blocking/permeabilization solution. Specimen were then incubated with Alexa Fluor secondary antibodies in PBS at room temperature for 1–2 h. Hoechst 33242 was used for nuclear counterstaining. Alexa-Fluor-conjugated phalloidin was paired with secondary antibodies in some cases to label actin-rich hair bundles. Each preparation was mounted with ProLong Gold Antifade Mountant prior to imaging.

### Preparation and imaging of X-gal-stained specimen

Cochlear whole mounts from RARE-lacZ hemizygous mice and whole RARE-lacZ aggregates from organoid cultures were fixed with 4% paraformaldehyde and 0.5% glutaraldehyde. In some cases, aggregates were cryopreserved as above and sectioned prior to X-gal staining. Specimens were permeabilized in wash buffer composed of 0.02% NP-40 and 0.01% sodium-deoxycholate in

phosphate buffer with 2 mM $MgCl_2$. Pre-warmed X-gal stain was prepared as 1 mg/mL X-gal in dimethylformamide in a buffer solution of 5 mM potassium ferrocyanide and 5 mM potassium ferricyanide. Preparations were incubated in this staining solution overnight in a humidified chamber at 37°C. After washing extensively, samples were counterstained in Nuclear Fast Red for 5 min at room temperature followed by PBS wash and imaging under phase contrast.

To quantify X-gal staining, cryosections from D13 to D14 aggregates were stained, imaged, and analyzed in ImageJ, tracing the epithelium of the OV with a freehand line tool with line thickness set to match epithelium thickness. Outlines were drawn counterclockwise, starting from a point closest to the centroid of the aggregate. Intensity profiles were normalized to polar coordinates and values averaged in 10° bins.

### Manipulation of RA signaling

Whole aggregates were exposed to inhibitors of RA signaling and/or exogenous atRA at various points in the IEO protocol. RA activity was reduced by the pan-RAR inverse agonist AGN193109 (0.1 μM) or inhibitors to RA synthesis with WIN18446 (5 μM; Aldh1a2 specific), 673A (50 μM; Aldh1a family specific), or 646 (1 μM; Aldha1-3 selective). Inhibitors and atRA were applied in media exchanges at indicated times and washed out by daily half-media exchanges. Vehicle for atRA, AGN193109, WIN18446, 673A, and 646 was dimethyl sulfoxide at a final concentration of 0.1% or less.

### Imaging

Brightfield imaging was accomplished on standard stereomicroscopes or Leica DM IL/LB compound microscopes outfitted with digital cameras (QImaging QICam or MicroPublisher). Epifluorescence imaging was achieved with an Olympus BX51WI microscope and Orca-Flash 4.0 cooled CCD camera (Hamamatsu). Confocal imaging was performed using an Olympus FluoView 1000 or Leica SP8 Lightning microscope.

### Statistical analysis

Comparisons between two group means were performed using unpaired t tests. Comparisons among more than 2 groups were performed with one-way or two-way ANOVA and post-hoc tests in SPSS 24 or GraphPad Prism 10.

## RESOURCE AVAILABILITY

### Lead contact

Requests for further information and resources should be directed to and will be fulfilled by the lead contact, R. Keith Duncan (rkduncan@umich.edu).

### Materials availability

Mouse cell lines generated in this study are available from the corresponding author with a completed materials transfer agreement. Key resources can be found in Table S4.

### Data and code availability

The acccession number for the RNA-seq analysis reported in this paper is GEO: GSE285576. All other data are available from the corresponding author.

## ACKNOWLEDGMENTS

This work was supported by a grant from the Veterans Administration (I01 RX003400 to R.K.D.). The authors thank Matthew Adams, Dr. Stacy Schaefer, and Dr. Joerg Waldhaus for assistance with some specimens and comments on early drafts of the manuscript.

## AUTHOR CONTRIBUTIONS

R.K.D. conceived and performed experiments, wrote the manuscript, and secured funding; L.L., M.M., A.W., R.D., and L.C. conducted the experiments.

## DECLARATION OF INTERESTS

The authors declare no competing interests.

## SUPPLEMENTAL INFORMATION

Supplemental information can be found online at https://doi.org/10.1016/j.stemcr.2025.102671.

Received: March 20, 2025
Revised: August 29, 2025
Accepted: September 5, 2025
Published: October 2, 2025

## REFERENCES

Afgan, E., Baker, D., Batut, B., van den Beek, M., Bouvier, D., Cech, M., Chilton, J., Clements, D., Coraor, N., Grüning, B.A., et al. (2018). The Galaxy platform for accessible, reproducible and collaborative biomedical analyses: 2018 update. Nucleic Acids Res. *46*, W537–W544.

Anders, S., Pyl, P.T., and Huber, W. (2015). HTSeq–a Python framework to work with high-throughput sequencing data. Bioinformatics *31*, 166–169.

Andrews, S. (2010). A quality control tool for high throughput sequence data. http://www.bioinformatics.babraham.ac.uk/projects/fastqc/.

Bok, J., Raft, S., Kong, K.A., Koo, S.K., Dräger, U.C., and Wu, D.K. (2011). Transient retinoic acid signaling confers anterior-posterior polarity to the inner ear. Proc. Natl. Acad. Sci. USA *108*, 161–166.

Burton, Q., Cole, L.K., Mulheisen, M., Chang, W., and Wu, D.K. (2004). The role of Pax2 in mouse inner ear development. Dev. Biol. *272*, 161–175.

Cassinotti, L.R., Ji, L., Yuk, M.C., Desai, A.S., Cass, N.D., Amir, Z.A., and Corfas, G. (2024). Hidden hearing loss in a Charcot-Marie-Tooth type 1A mouse model. JCI Insight *9*, e180315.

de Hoon, M.J.L., Imoto, S., Nolan, J., and Miyano, S. (2004). Open source clustering software. Bioinformatics *20*, 1453–1454.

DeJonge, R.E., Liu, X.P., Deig, C.R., Heller, S., Koehler, K.R., and Hashino, E. (2016). Modulation of Wnt Signaling Enhances Inner Ear Organoid Development in 3D Culture. PLoS One *11*, e0162508.

Donato, M., Xu, Z., Tomoiaga, A., Granneman, J.G., Mackenzie, R. G., Bao, R., Than, N.G., Westfall, P.H., Romero, R., and Draghici, S. (2013). Analysis and correction of crosstalk effects in pathway analysis. Genome Res. *23*, 1885–1893.

Draghici, S., Khatri, P., Tarca, A.L., Amin, K., Done, A., Voichita, C., Georgescu, C., and Romero, R. (2007). A systems biology approach for pathway level analysis. Genome Res. *17*, 1537–1545.

Durruthy-Durruthy, R., Gottlieb, A., Hartman, B.H., Waldhaus, J., Laske, R.D., Altman, R., and Heller, S. (2014). Reconstruction of the mouse otocyst and early neuroblast lineage at single-cell resolution. Cell *157*, 964–978.

Flagiello, D., Gibaud, A., Dutrillaux, B., Poupon, M.F., and Malfoy, B. (1997). Distinct patterns of all-trans retinoic acid dependent expression of HOXB and HOXC homeogenes in human embryonal and small-cell lung carcinoma cell lines. FEBS Lett. *415*, 263–267.

Frenz, D.A., Liu, W., Cvekl, A., Xie, Q., Wassef, L., Quadro, L., Niederreither, K., Maconochie, M., and Shanske, A. (2010). Retinoid signaling in inner ear development: A "Goldilocks" phenomenon. Am. J. Med. Genet. *152A*, 2947–2961.

Groves, A.K., and Fekete, D.M. (2012). Shaping sound in space: the regulation of inner ear patterning. Development *139*, 245–257.

Heanue, T.A., Davis, R.J., Rowitch, D.H., Kispert, A., McMahon, A. P., Mardon, G., and Tabin, C.J. (2002). Dach1, a vertebrate homologue of Drosophila dachshund, is expressed in the developing eye and ear of both chick and mouse and is regulated independently of Pax and Eya genes. Mech. Dev. *111*, 75–87.

Hocevar, S.E., Liu, L., and Duncan, R.K. (2021). Matrigel is required for efficient differentiation of isolated, stem cell-derived otic vesicles into inner ear organoids. Stem Cell Res. *53*, 102295.

Huddle, B.C., Grimley, E., Buchman, C.D., Chtcherbinine, M., Debnath, B., Mehta, P., Yang, K., Morgan, C.A., Li, S., Felton, J., et al. (2018). Structure-Based Optimization of a Novel Class of Aldehyde Dehydrogenase 1A (ALDH1A) Subfamily-Selective Inhibitors as Potential Adjuncts to Ovarian Cancer Chemotherapy. J. Med. Chem. *61*, 8754–8773.

Jia, S., and Meng, A. (2021). TGFbeta family signaling and development. Development *148*, dev188490.

Kiernan, A.E., Pelling, A.L., Leung, K.K.H., Tang, A.S.P., Bell, D.M., Tease, C., Lovell-Badge, R., Steel, K.P., and Cheah, K.S.E. (2005). Sox2 is required for sensory organ development in the mammalian inner ear. Nature *434*, 1031–1035.

Kim, D., Langmead, B., and Salzberg, S.L. (2015). HISAT: a fast spliced aligner with low memory requirements. Nat. Methods *12*, 357–360.

Koehler, K.R., Mikosz, A.M., Molosh, A.I., Patel, D., and Hashino, E. (2013). Generation of inner ear sensory epithelia from pluripotent stem cells in 3D culture. Nature *500*, 217–221.

Kwon, H.J., Bhat, N., Sweet, E.M., Cornell, R.A., and Riley, B.B. (2010). Identification of early requirements for preplacodal ectoderm and sensory organ development. PLoS Genet. *6*, e1001133.

Laurikkala, J., Mikkola, M.L., James, M., Tummers, M., Mills, A.A., and Thesleff, I. (2006). p63 regulates multiple signalling pathways required for ectodermal organogenesis and differentiation. Development *133*, 1553–1563.

Love, M.I., Huber, W., and Anders, S. (2014). Moderated estimation of fold change and dispersion for RNA-seq data with DESeq2. Genome Biol. *15*, 550.

Martin, M. (2011). Cutadapt removes adapter sequences from high-throughput sequencing reads. EMBnet. j. *17*, 10–12.

Matern, M.S., and Heller, S. (2025). A developmental atlas of mouse vestibular-like inner ear organoids. iScience *28*, 111817.

Moore, S.T., Nakamura, T., Nie, J., Solivais, A.J., Aristizábal-Ramírez, I., Ueda, Y., Manikandan, M., Reddy, V.S., Romano, D.R., Hoffman, J.R., et al. (2023). Generating high-fidelity cochlear organoids from human pluripotent stem cells. Cell Stem Cell *30*, 950–961.e7.

Morsli, H., Tuorto, F., Choo, D., Postiglione, M.P., Simeone, A., and Wu, D.K. (1999). Otx1 and Otx2 activities are required for the normal development of the mouse inner ear. Development *126*, 2335–2343.

Nauryzgaliyeva, Z., Goux Corredera, I., Garreta, E., and Montserrat, N. (2023). Harnessing mechanobiology for kidney organoid research. Front. Cell Dev. Biol. *11*, 1273923.

Niederreither, K., and Dollé, P. (2008). Retinoic acid in development: towards an integrated view. Nat. Rev. Genet. *9*, 541–553.

Noda, T., Oki, S., Kitajima, K., Harada, T., Komune, S., and Meno, C. (2012). Restriction of Wnt signaling in the dorsal otocyst determines semicircular canal formation in the mouse embryo. Dev. Biol. *362*, 83–93.

Ohta, S., Wang, B., Mansour, S.L., and Schoenwolf, G.C. (2016). BMP regulates regional gene expression in the dorsal otocyst through canonical and non-canonical intracellular pathways. Development *143*, 2228–2237.

Orvis, J., Gottfried, B., Kancherla, J., Adkins, R.S., Song, Y., Dror, A. A., Olley, D., Rose, K., Chrysostomou, E., Kelly, M.C., et al. (2021). gEAR: Gene Expression Analysis Resource portal for community-driven, multi-omic data exploration. Nat. Methods *18*, 843–844.

Radde-Gallwitz, K., Pan, L., Gan, L., Lin, X., Segil, N., and Chen, P. (2004). Expression of Islet1 marks the sensory and neuronal lineages in the mammalian inner ear. J. Comp. Neurol. *477*, 412–421.

Romand, R., Kondo, T., Fraulob, V., Petkovich, M., Dollé, P., and Hashino, E. (2006). Dynamic expression of retinoic acid-synthesizing and -metabolizing enzymes in the developing mouse inner ear. J. Comp. Neurol. *496*, 643–654.

Saldanha, A.J. (2004). Java Treeview–extensible visualization of microarray data. Bioinformatics *20*, 3246–3248.

Schaefer, S.A., Higashi, A.Y., Loomis, B., Schrepfer, T., Wan, G., Corfas, G., Dressler, G.R., and Duncan, R.K. (2018). From Otic Induction to Hair Cell Production: Pax2(EGFP) Cell Line Illuminates

Key Stages of Development in Mouse Inner Ear Organoid Model. Stem Cells Dev. *27*, 237–251.

van der Valk, W.H., van Beelen, E.S.A., Steinhart, M.R., Nist-Lund, C., Osorio, D., de Groot, J.C.M.J., Sun, L., van Benthem, P.P.G., Koehler, K.R., and Locher, H. (2023). A single-cell level comparison of human inner ear organoids with the human cochlea and vestibular organs. Cell Rep. *42*, 113527.

Vitelli, F., Viola, A., Morishima, M., Pramparo, T., Baldini, A., and Lindsay, E. (2003). TBX1 is required for inner ear morphogenesis. Hum. Mol. Genet. *12*, 2041–2048.

Vyas, B., Nandkishore, N., and Sambasivan, R. (2020). Vertebrate cranial mesoderm: developmental trajectory and evolutionary origin. Cell. Mol. Life Sci. *77*, 1933–1945.

Waldhaus, J., Jiang, L., Liu, L., Liu, J., and Duncan, R.K. (2024). Mapping the developmental potential of mouse inner ear organoids at single-cell resolution. iScience *27*, 109069.

Wang, W., Grimmer, J.F., Van De Water, T.R., and Lufkin, T. (2004). Hmx2 and Hmx3 homeobox genes direct development of the murine inner ear and hypothalamus and can be functionally replaced by Drosophila Hmx. Dev. Cell *7*, 439–453.

Wu, D.K., and Kelley, M.W. (2012). Molecular mechanisms of inner ear development. Cold Spring Harb. Perspect. Biol. *4*, a008409.

Xu, Q., and Kopp, J.B. (2012). Retinoid and TGF-beta families: crosstalk in development, neoplasia, immunity, and tissue repair. Semin. Nephrol. *32*, 287–294.

Xu, Y., Zhang, Y., and Lundberg, Y.W. (2016). Spatiotemporal differences in otoconial gene expression. Genesis *54*, 613–625.

Zheng, W., Huang, L., Wei, Z.B., Silvius, D., Tang, B., and Xu, P.X. (2003). The role of Six1 in mammalian auditory system development. Development *130*, 3989–4000.